

JES Focus Issue on Lithium-Sulfur Batteries: Materials, Mechanisms, Modeling, and Applications

# Operando Spectromicroscopy of Sulfur Species in Lithium-Sulfur Batteries

Elizabeth C. Miller, <sup>®</sup> a,\* Robert M. Kasse, <sup>®</sup> a,b Khloe N. Heath, a Brian R. Perdue, and Michael F. Toney <sup>®</sup> a,z

In this study, a novel cross-sectional battery cell was developed to characterize lithium-sulfur batteries using X-ray spectromicroscopy. Chemically sensitive X-ray maps were collected operando at energies relevant to the expected sulfur species and were used to correlate changes in sulfur species with electrochemistry. Significant changes in the sulfur/carbon composite electrode were observed from cycle to cycle including rearrangement of the elemental sulfur matrix and  $PEO_{10}$ LiTFSI binder. Polysulfide concentration and area of spatial diffusion increased with cycling, indicating that some polysulfide dissolution is irreversible, leading to polysulfide shuttle. Fitting of the maps using standard sulfur and polysulfide XANES spectra indicated that upon subsequent discharge/charge cycles, the initial sulfur concentration was not fully recovered; polysulfides and lithium sulfide remained at the cathodes with higher order polysulfides as the primary species in the region of interest. Quantification of the polysulfide concentration across the electrolyte and electrode interfaces shows that the polysulfide concentration before the first discharge and after the third charge is constant within the electrolyte, but while cycling, a significant increase in polysulfides and a gradient toward the lithium metal anode forms. This chemically and spatially sensitive characterization and analysis provides a foundation for further operando spectromicroscopy of lithium-sulfur batteries.

© The Author(s) 2017. Published by ECS. This is an open access article distributed under the terms of the Creative Commons Attribution 4.0 License (CC BY, http://creativecommons.org/licenses/by/4.0/), which permits unrestricted reuse of the work in any medium, provided the original work is properly cited. [DOI: 10.1149/2.0091801jes] All rights reserved.

Manuscript submitted August 22, 2017; revised manuscript received October 10, 2017. Published November 3, 2017. This paper is part of the JES Focus Issue on Lithium-Sulfur Batteries: Materials, Mechanisms, Modeling, and Applications.

New "beyond lithium-ion" battery chemistries are essential to meet the increasing demand for long-lasting, high capacity energy storage in portable electronics and electric vehicles. Lithium-sulfur (Li-S) batteries are an attractive Li-ion alternative that provides large capacity (1672 mAh g $^{-1}$ ) and energy density (2500 Wh kg $^{-1}$ ) while also being low cost, earth-abundant, and lightweight.  $^{1-3}$  Li-S batteries have a unique chemistry that achieves high capacity via chemical transformation rather than Li intercalation. Elemental sulfur (S $_8$ ) is reduced through a series of soluble Li polysulfides (Li $_2$ S $_x$ , 2  $\leq$  x  $\leq$  8) to a final solid discharge product (Li $_2$ S), and the process is reversed upon charging.  $^{4-6}$  However, Li-S suffers from unrealized theoretical capacity and rapid capacity fade due to loss processes that are not well-understood.  $^{2,7}$ 

While many advances in electrode and electrolyte engineering have been made in an attempt mitigate these performance issues, 8-14 a gap remains in the mechanistic understanding of Li-S battery operation. Several mechanisms for reduced capacity and capacity fade have been proposed. Lithium polysulfides, which are necessary for operation, dissolve into the liquid electrolyte, remain dissolved, and "shuttle" between the electrodes rather than participating in the electrochemical reactions, decreasing the amount of active material available. 3,15-18 Low sulfur utilization results in initially low capacity that then continues to decrease with subsequent cycles. 19-21 Batteries are spatially and chemically heterogeneous, and deciphering the speciation and distribution of dissolved polysulfides in the anode, cathode, and especially the electrolyte during cycling is critical for realizing the potential of Li-S.

The best way to capture an accurate picture of battery electrochemistry is using operando or in situ characterization. <sup>22,23</sup> Ex situ methods, while useful, do not provide the direct, in situ knowledge of the dissolved polysulfides that is required to determine where and when specific species form. Polysulfides can disproportionate with time, <sup>24,25</sup> and so capturing the species immediately after they form is critical to determining battery behavior. Because of the unique insight they provide, operando techniques are critical to understanding all energy storage systems but especially the chemistry of Li-S batteries.

Methods such as nuclear magnetic resonance, <sup>26,27</sup> Raman<sup>28,29</sup> and UV/Vis<sup>30,31</sup> spectroscopy have been used to characterize lithium polysulfides both ex situ and in situ. X-ray diffraction<sup>32–34</sup> and X-ray absorption spectroscopy (XAS)<sup>35–39</sup> have been used for operando experiments that focus on polysulfides, giving bulk, non-spatially resolved information. Transmission X-ray microscopy<sup>33,40</sup> provides spatiallyresolved microstructural information but lacks the ability to provide chemical information at the sulfur K-edge due to the hard X-ray energies needed for imaging. Methods such as first principles have been used to generate "standard" polysulfide X-ray spectra to isolate individual species before disproportionation<sup>41,42</sup> as a complement to operando studies and verification of experimental data. Microprobe XAS, which uses a beam size on the order of microns rather than millimeters, as is commonly the case for XAS, can provide more targeted, spatially resolved information. Several of these spectra can be stitched together to create a spatially sensitive picture, yet this method does not provide a visualization of the chemistry that can be directly correlated to the structure and chemistry of the battery electrode. In addition, most X-ray characterization is performed through the thickness of the battery electrodes, giving an average of the chemistry throughout the cell. While some cross-sectional work has been done, <sup>36,37</sup> it has been limited to XAS rather than spectromicroscopy experiments.

In this paper, we present X-ray spectromicroscopy of a crosssectional Li-S battery that presents a spatially resolved chemical picture of the electrodes and electrolyte during galvanostatic cycling. From these measurements, the condition of the electrode at different states of charge can be qualitatively compared; furthermore, with the use of standards and image processing methods, the concentrations of sulfur species can be quantitatively analyzed. We find that the species present at five representative time points during cycling vary dramatically but ultimately confirm the mechanistic picture of polysulfide reduction and oxidation. Additionally, a concentration gradient from the cathode to the anode forms during cycling but disappears after the

<sup>&</sup>lt;sup>a</sup>Stanford Synchrotron Radiation Lightsource, SLAC National Accelerator Laboratory, Menlo Park, California 94025, USA

<sup>&</sup>lt;sup>b</sup>Department of Materials Science & Engineering, Stanford University, Stanford, California 94305, USA

<sup>&</sup>lt;sup>c</sup> Joint Center for Energy Storage Research, Sandia National Laboratories, Albuquerque, New Mexico 87185, USA

<sup>\*</sup>Electrochemical Society Student Member.

<sup>&</sup>lt;sup>z</sup>E-mail: mftoney@slac.stanford.edu

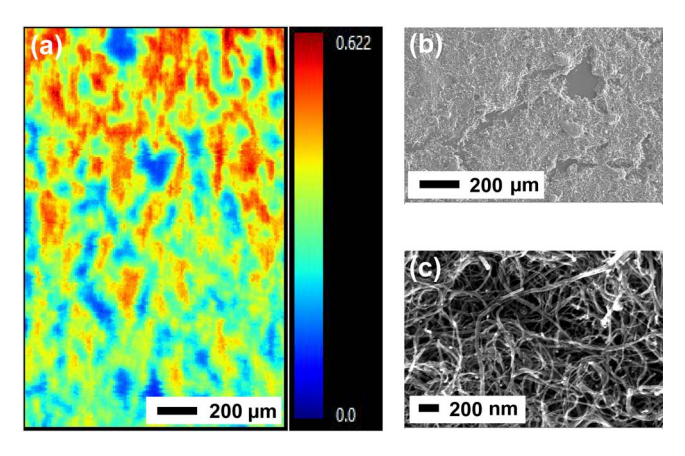


**Figure 1.** X-ray spectromicroscopy map (a) and scanning electron microscope images ((b) and (c)) of the as-prepared electrode. The electrode is laterally homogeneous on a scale relevant to this experiment although the sulfur coverage is non-uniform

final cycle. Ultimately, we can conclude that polysulfide dissolution is not completely reversible and that higher order polysulfides are the primary species after the final charge.

## **Experimental**

Electrode preparation.—The sulfur/PEO<sub>10</sub>LiTFSI cathodes were prepared according to the following procedure. Using a mortar and pestle, 80 wt% sulfur (Aldrich) was combined with 20 wt% 10-20 nm bulk carbon nanotubes (CNT) and mixed thoroughly. The mixture was added to a round bottom flask and was evacuated to less than 50 mTorr. The round bottom flask was then placed in an oven and heated to  $150^{\circ} C$ for a minimum of 18 h. The resulting S/CNT composite was reground in a mortar and pestle to break up large particulates and then ball milled in a planetary mill for a minimum of 18 h. The PEO<sub>10</sub>LiTFSI binder was prepared by first mixing 60 wt% 4M mw poly(ethylene oxide) (PEO, Aldrich) with 40 wt% bis(trifluoromethane)sulfonimide lithium salt (LiTFSI, Aldrich), and then sufficient acetonitrile (ACN, Aldrich) was added to produce a maximum of 4 wt% solution (based on total mass of PEO+LiTFSI). Cathode slurries were prepared by mixing 80 wt% S/CNT, 10 wt% PEO<sub>10</sub>LiTFSI, and 10 wt% Super P carbon black (TIMCAL) in ACN and in a Cowles mixer/blender until homogenized. The slurry was coated onto a carbon coated aluminum foil current collector (Intellicoat) using a doctor blade with an elcometer. Films were coated at 500 µm wet film thickness, dried overnight in atmosphere, and then placed under vacuum overnight. The resulting coatings have an average loading of 6 mg cm<sup>-2</sup> sulfur and a composition of 64 wt% S/26 wt% carbon/10 wt% binder. The electrodes were examined using scanning electron microscopy (SEM, Zeiss) and X-ray spectromicroscopy to determine the quality of the film. These images are shown in Figure 1. In the spectromicroscopy image Figure 1a, areas of red indicate higher sulfur concentration, and areas of dark blue indicate less sulfur. The SEM image at the same scale as the X-ray image is shown in Figure 1b with a higher resolution image of the carbon matrix shown in Figure 1c. In Figures 1a and 1b, it can be seen that the sulfur loading in not continuous, but the film is laterally homogeneous. Figure 1c shows the carbon matrix is well-connected and homogeneous. Thus, the film is homogeneous on the scale relevant to this experiment even if the sulfur is not continuous. The dried thickness of the film is  $\sim$ 90  $\mu$ m as confirmed by micrometer measurements.

Operando cell design & battery fabrication.—The cross-sectional geometry of the cell is critical to this experiment because it provides insight into the diffusion of sulfur species in a unique way that cannot be captured in more conventional pouch or coin cells. The goal of this sample design is to obtain the electrochemistry of a coin cell

while maintaining the X-ray compatibility of a pouch cell. Thus, the fabrication of the cell needed to be adjusted accordingly for the new geometry.

The sulfur electrode was cut into a rectangle (active area = 0.63 cm²) using a razor blade. An equivalent size of lithium foil (Sigma-Aldrich) was used as the counter electrode. The electrolyte solution consisted of 1 M lithium perchlorate (LiClO<sub>4</sub>, Sigma-Aldrich) and 0.2 M lithium nitrate (LiNO<sub>3</sub>, Sigma-Aldrich) in a 1:1 mixture by volume of 1,3-dioxolane and 1,2-dimethoxyethane (DOL/DME, Sigma-Aldrich).

The cell was assembled in a cross-sectional geometry using a custom-designed polyether ether ketone (PEEK) electrochemical cell. Schematic drawings and photos of the front (a, c), inside (b, d), and top (e) of the cell are shown in Figure 2. A 1 mm square, 100 nm thick silicon nitride membrane on a 10 mm square silicon frame (TEMwindows) was affixed to the PEEK cell using a polyolefin adhesive (Superchlon). Silicon nitride windows were used because they offer very high X-ray transmission in the tender X-ray regime between roughly 1500 eV and 5000 eV where the sulfur K-edge (2472 eV) falls. The window was mounted with the silicon nitride membrane facing the battery assembly to prevent the lithiation of the silicon frame holding the membrane. The cell was assembled in an argon glove box containing < 0.5 ppm H<sub>2</sub>O and < 0.20 ppm O<sub>2</sub>. The battery was oriented so that the sulfur cathode was on the left-hand side and the lithium was on the right-hand side when looking through the X-ray window from the front of the cell. Two glass fiber separators (Whatman GF/C) were used instead of one separator to maximize the area for mapping between the electrodes and to increase the pressure on the battery assembly. Stainless steel screws were used to apply pressure for electrode contact as well as to act as current collectors/electrical contacts. Electrolyte was injected using a syringe through the ports on the top of the cell. Once assembled, the cell was sealed in argon before being removed from the glove box. The sample was transferred to a helium sample environment at the beamline with minimal exposure to air.

*Electrochemical characterization.*—The cross-sectional cell was cycled under a constant current of 0.38 mA cm<sup>-2</sup> (nominal C/20 rate based on theoretical capacity of Li-S) between voltage cutoffs of 1.5 and 3.4 V using a potentiostat (SP150, Bio-Logic Science Instruments) and the EC-Lab software package. The open circuit voltage (OCV) of the cell was 2.42 V, which is within the range of 2.3–2.6 V that is reported in literature. <sup>43,44</sup> Three discharge/charge cycles were completed on the beamline during a 24 h period.

*X-ray characterization.*—X-ray absorption spectroscopy (XAS) was performed at beamline 14-3 at the Stanford Synchrotron Radiation Lightsource of SLAC National Accelerator Laboratory. X-ray absorption near edge structure (XANES) and X-ray spectromicroscopy were performed at the sulfur K-edge using a Vortex detector (Hitachi) in a fluorescence geometry. A helium sample environment increased the incident beam by decreasing X-ray absorption from air. By maximizing the incident beam, fewer scans are required to obtain adequate signal, which mitigates beam damage. Additionally, beam damage was assessed by continuously exposing one region to the X-ray beam and monitoring for changes. No damage was observed. Maps were collected with a 15 µm step size, 50 ms dwell time, and 5 µm spot size. The sample was scanned from left to right, starting in the lower left-hand corner of the image and ending in the upper right-hand corner. During cycling, multi-energy maps were collected at five selected energies to allow for species identification. All energies were collected for one line in the image before moving to the next line, and each set of five maps took approximately 80 minutes to collect. Spectromicroscopy maps were analyzed using the MicroAnalysis Toolkit (Sam's Microprobe Analysis Kit, or SMAK),45 and XANES spectra were analyzed using the Athena X-ray absorption spectroscopy program.46

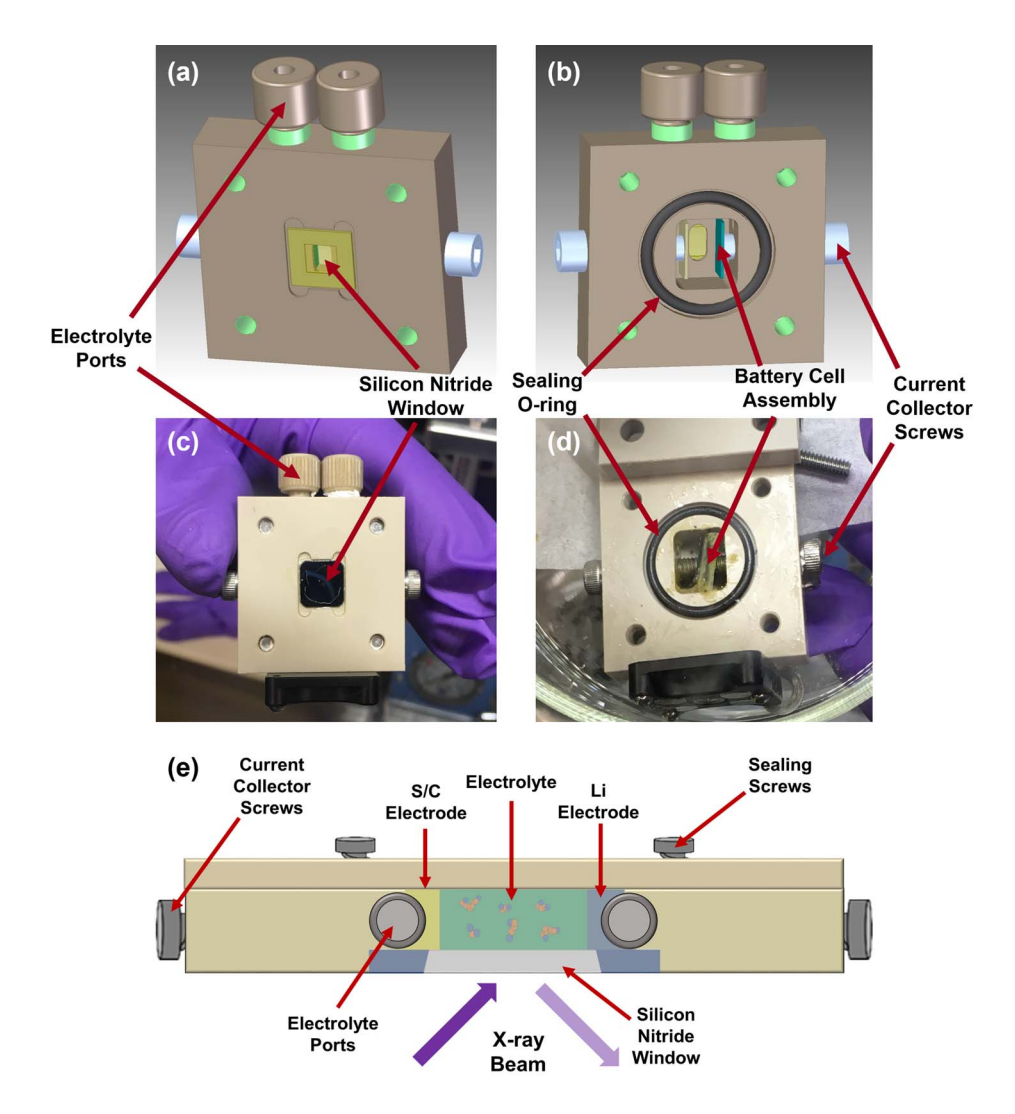


Figure 2. Schematic drawings and photos of the front ((a) and (c)), inside ((b) and (d)), and top (e) of the cross-sectional cell design used for X-ray spectromicroscopy. The view from the top of the cell (e) also shows the incident X-ray beam on the silicon nitride window as well as the cross-section of the cell assembly.

## **Results and Discussion**

*Operando imaging & electrochemistry.*—Maps were collected at 2470.35 eV, 2472.6 eV, 2480.6 eV, and 2500 eV to represent polysulfides, elemental sulfur, the sulfonyl (sulfur atom double bonded to two oxygen atoms) group in LiTFSI included in the binder, and "total" sulfur (a value above the edge where all sulfur species are excited), respectively. An additional map was collected at 2477.5 eV, which corresponds to a higher order polysulfide spectral feature, to aid in fitting (discussed in the "XANES Fitting" section). These values were taken from literature  $^{35-37,41}$  as well as from spectra taken in this experiment at various points on the battery cell before cycling. These energies are denoted on an  $S_8$  standard spectrum in Figure 3. Although LiTFSI is often used as the electrolyte salt in the Li-S system, here LiClO $_4$  salt was used instead so that it is known that any sulfur signal originates from the electrode or binder rather than the salt. This chemistry has been demonstrated previously with X-ray absorption spectroscopy experiments.  $^{36,37}$ 

The discharge and charge curves of the battery are presented in Figure 4. The points at which maps were collected are marked with dots of corresponding color on each curve and labeled (a) through (r) in order of collection. A schematic of the cell with the lines that show the layers of the battery stack is also shown. Images (a) through (i) in Figure 4 (below the voltage vs. capacity graph) are the maps

taken at 2470.35 eV, representative of soluble polysulfides, during the first discharge/charge cycle and demonstrate the significant changes that occur during cycling. The discontinuities observed in images (c) through (h) are real effects caused by chemical processes in the electrode occurring at a faster rate than the 15  $\mu m$  step size and 50 ms dwell time could capture. This observation was present in every energy at a given time point and was verified by examining the signal of the incident X-ray beam, which was uninterrupted during data collection. Thus, the effect originated in the sample and not the experimental setup.

The maximum capacity of the cross-sectional cell on the first discharge cycle is 570 mAh g<sup>-1</sup>. Because the current collector screws are applying pressure to an area smaller than the total area of the electrode (i.e. just the area of the screw bottom and any pressure that was applied to the stack during cell assembly), it is possible that the contact area between the electrodes is smaller than the assumed 0.63 cm<sup>2</sup> total area of the electrode. Thus, less active material may be available to participate in the reaction, leading to reduced capacity and decreased cycling time. Additionally, the plateaus during discharge appear at 2.0 and 1.8 V, which is lower than the typically observed 2.4 and 2.1 V. However, two plateaus are still observed without additional features in the curve, indicating that the two expected polysulfide reduction processes are present, likely without additional side reactions.

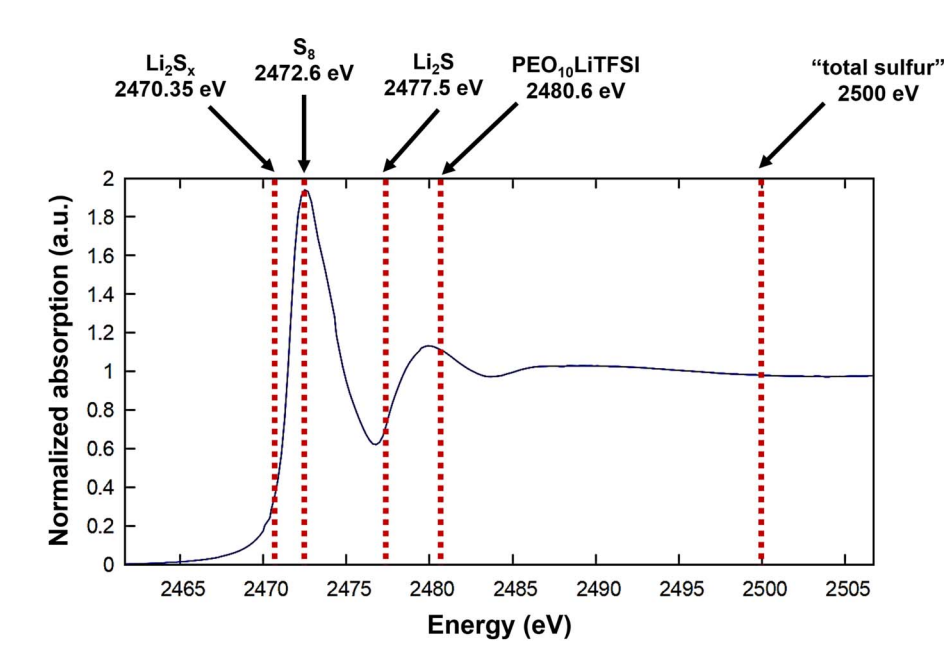


**Figure 3.** Energies chosen for multi-energy operando mapping. The corresponding chemistry at each energy is indicated on an S<sub>8</sub> standard spectrum shown for reference.

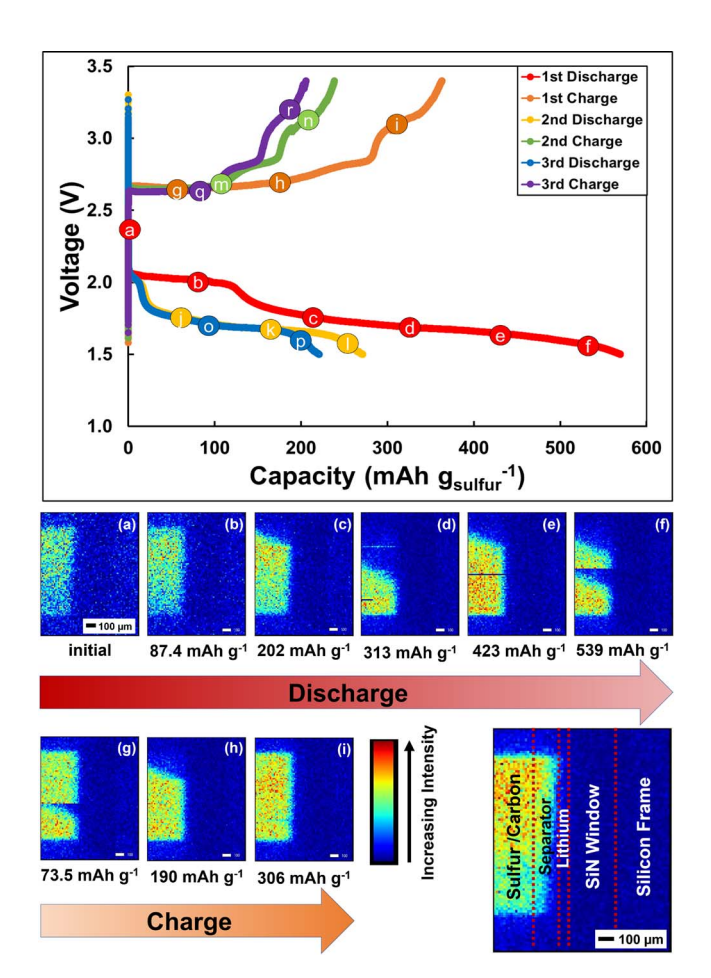


**Figure 4.** Charge/discharge curves from operando characterization of the cross-sectional cell. Points at which maps were collected are marked with colored dots labeled (a) through (r). Maps taken at 2470.35 eV representing the polysulfides are shown below the graph during the first discharge (red curve, images (a) through (f)) and charge (orange curve, images (g) through (i)). The approximate location of the battery stack components in the images are shown in the lower right-hand corner.

In previous reports, <sup>47</sup> increased porosity of the electrode was found to decrease the voltage plateaus in the discharge curves for the same discharge rates; additionally, overall capacity decreased, likely due to higher resistances and lower conductivity resulting from a more porous film. As seen in Figure 1, the electrode has some regions where the film coverage is not as uniform, which may be an explanation for our electrochemical observations. Additionally, the higher porosity electrodes resulted in a larger "ohmic drop," the initial decrease from the OCV to the beginning of the discharge plateau,<sup>47</sup> due to higher internal resistance. This feature is observed in the electrochemistry shown in Figure 4. Higher current values used for cycling can result in lower discharge plateaus in both Li-ion<sup>48</sup> and Li-S<sup>49</sup> batteries. If the sulfur loading of the film is more heterogeneous than we can see with the X-ray and SEM analysis, then it is possible that there are local pockets of an effective higher current. This effect may also contribute to the depressed plateaus. To be sure of the cause, further investigation is required and will be pursued in future work.

Figure 5 shows the evolution of the polysulfides, elemental sulfur, and PEO<sub>10</sub>LiTFSI binder during the first discharge (Points (a) and (f)) and charge (Points (g) and (i)) as well as the final state after three discharge/charge cycles (Point (r)). The spatial extent of the sulfur species, specifically the polysulfides, increases from the initial state at Point (a) to the end of the first discharge at Point (f). Also, at Points (f) and (g), discontinuities in the electrode are observed, indicating structural changes that are not captured by the data acquisition rate. At the end of the first charge, labeled Point (i), most of the electrode structure of elemental sulfur and binder has been restored. However, the area of polysulfide diffusion remains expanded, indicating that the sulfur species remain dissolved in the electrolyte and trapped in the separator, even upon charge. This expansion is additional evidence of the polysulfide shuttle effect that is believed to cause capacity to fade.

After cycling, the sulfur electrode shows significant, irreversible changes in structure without any discontinuities. At Point (r), the electrode is no longer homogeneous and shows areas of high sulfur concentration and areas of little or no sulfur signal. The loss of active material in the maps correlates to the loss of capacity that is observed in second and third cycles.

**XANES fitting.**—Sulfur  $(S_8)$ , lithium sulfide  $(Li_2S)$ , and lithium polysulfide  $(Li_2S_x, x = 4, 6, 8)$  standards were collected at the same beamline to create a series of spectra for XANES fitting. Using a non-negative least squares fitting routine in SMAK, the maps taken at Points (a), (f), (g), (i), and (f) were fit using four normalized standards.

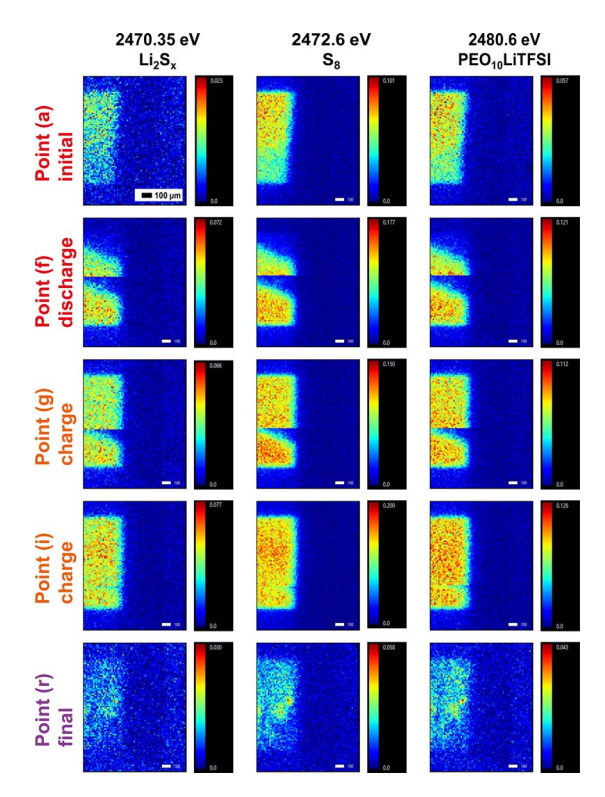


**Figure 5.** X-ray fluorescence maps of the first discharge (Point (a) and (f)), first charge (Point (g) and (i)), and final state after three cycles (Point (r)). Left to right, energies shown in each column correspond to polysulfides (2470.35 eV), elemental sulfur (2472.6 eV), and PEO<sub>10</sub>LiTFSI (2480.6 eV), respectively.

In order to provide a true representation of our observations and to avoid overfitting the data, the chemically similar  $\text{Li}_2S_4$  and  $\text{Li}_2S_6$  spectra were averaged, allowing four standards  $(S_8, \text{Li}_2S_8, \text{Li}_2S_6 + \text{Li}_2S_4, \text{Li}_2S)$  to be fit to five energy-specific maps (2470.35 eV, 2472.6 eV, 2477.5 eV, 2480.6 eV, 2500 eV) at each time point.

The fitting results are summarized in Figure 6. The map of "total" sulfur at 2500 eV where all sulfur species are excited is shown for reference on the left while the residual from fitting (error) is shown at the right. Fitting resulted in less than 2% residual in pixel intensity across all maps, showing excellent description of the data by our model. At Point (a), before the battery begins discharging, the majority species is S<sub>8</sub>. Simply from resting between the time of battery fabrication and the beginning of X-ray characterization, some higher order polysulfides have formed as evidenced by the intensity in the Li<sub>2</sub>S<sub>8</sub> and Li<sub>2</sub>S<sub>6</sub>+Li<sub>2</sub>S<sub>4</sub> standard maps; however, Li<sub>2</sub>S has not yet formed in any significant amount. From Point (a) to (f), more Li<sub>2</sub>S appears, which is expected, as Li<sub>2</sub>S forms when the battery discharges. However, the Li<sub>2</sub>S signal continues to increase from Point (f) to Point (g), the first point taken in the charge cycle, indicating a lag in formation of the polysulfide species with respect to the electrochemistry. That is, the conversion of long chain polysulfides to shorter chain polysulfides and lithium sulfide continues for a short period after the current is reversed, as the chemistry begins to catch up to the reversed electrochemistry. At the end of the first charge cycle, Point (i), some of the S<sub>8</sub> is recovered, but the XANES fitting indicates mostly Li<sub>2</sub>S<sub>8</sub> is present. Because not all of the initial S<sub>8</sub> intensity is recovered, it can be observed that the reaction is only quasi-reversible rather than fully reversible. This finding agrees qualitatively with previous X-ray studies 15,35 as well as studies made by other methods such as UV-Vis.<sup>31</sup> At the end of the third charge cycle, the majority of the species present are Li<sub>2</sub>S<sub>8</sub> with residual Li<sub>2</sub>S<sub>6</sub>+Li<sub>2</sub>S<sub>4</sub>, Li<sub>2</sub>S, and some S<sub>8</sub>. Even when the battery is charged, the Li<sub>2</sub>S end product does not entirely disappear, which is further evidence of the quasi-reversible nature of the reaction.

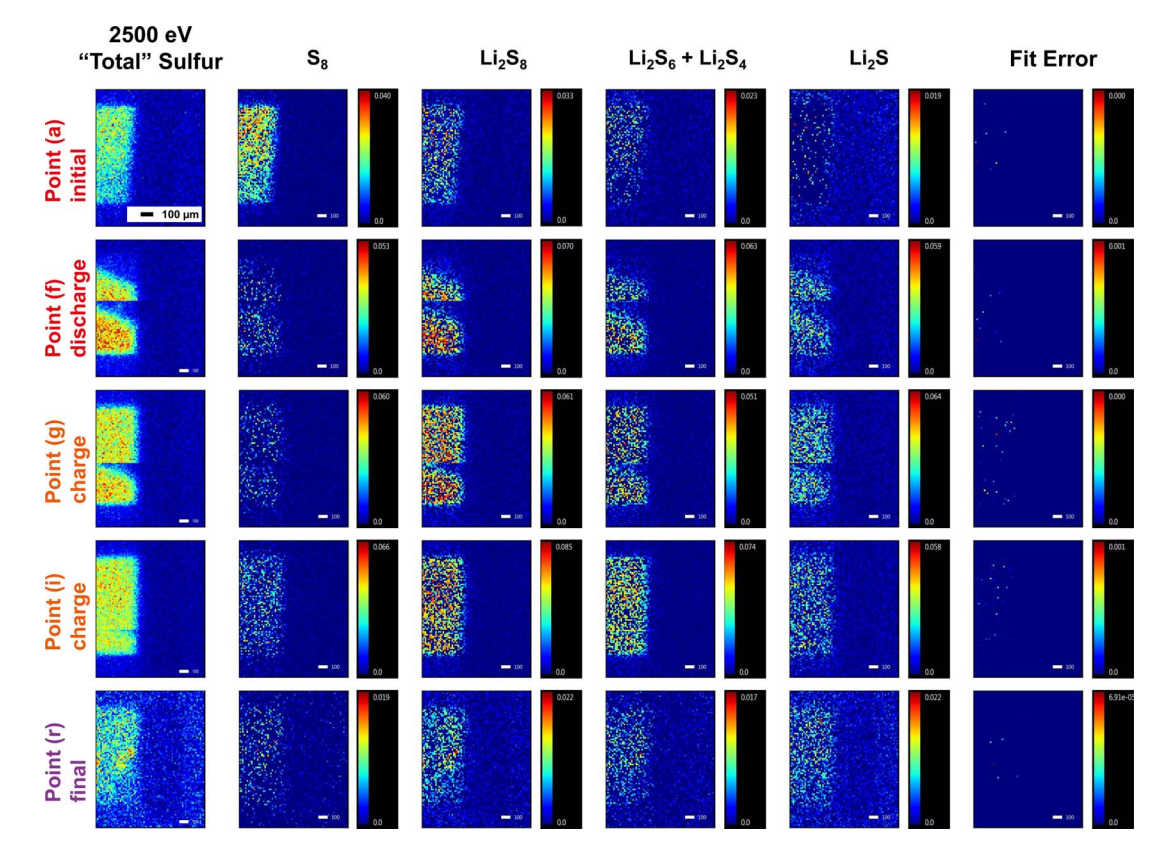


**Figure 6.** Fitting results from the first discharge (Points (a) and (f))/charge (Points (g) and (i)) cycle and the final state after three cycles (Point (r)). The "total" sulfur map at 2500 eV is shown at the left for reference, and the fit residual for each time point is shown at the right.

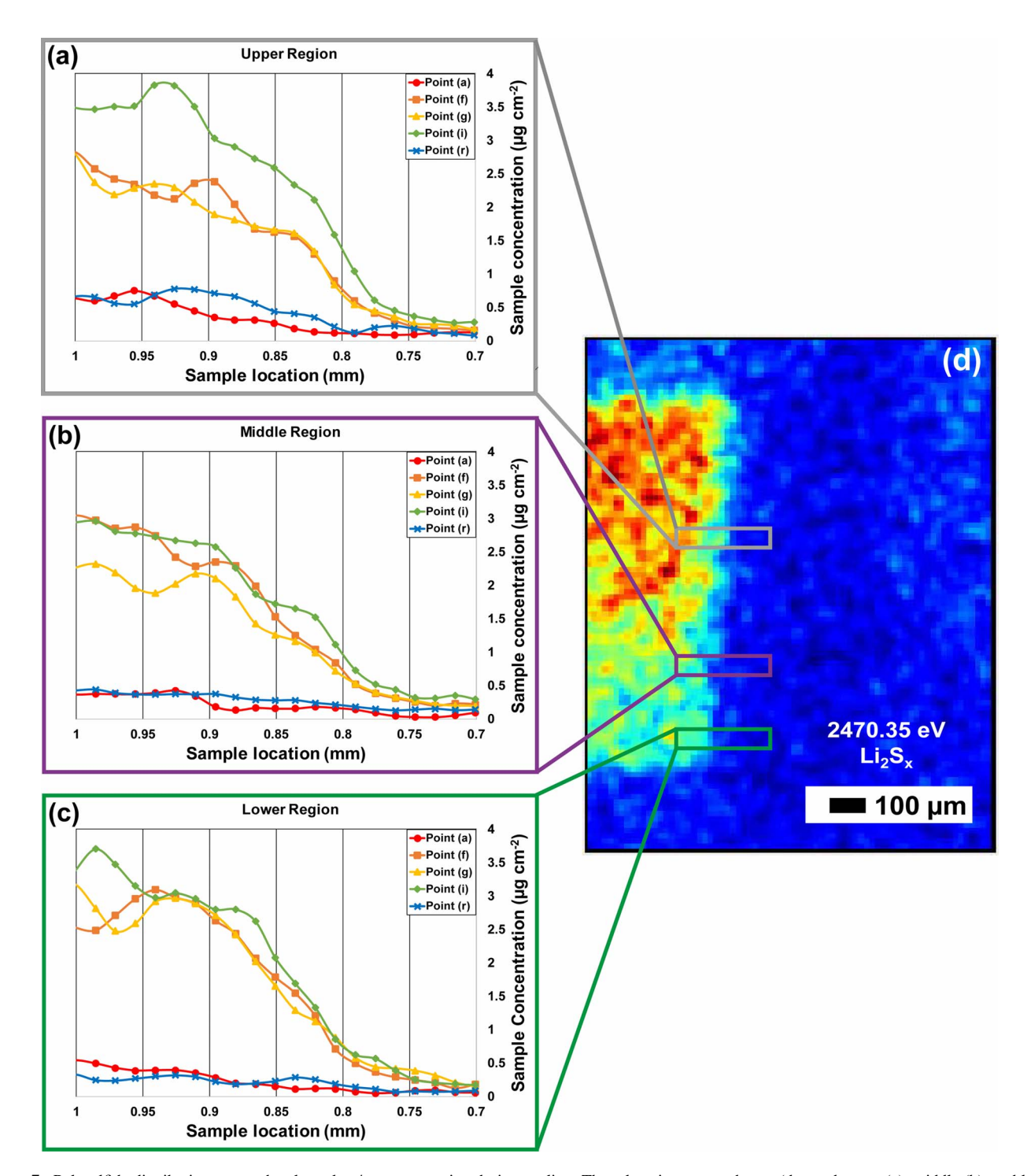


Figure 7. Polysulfide distribution across the electrolyte/separator region during cycling. Three locations were chosen (denoted upper (a), middle (b), and lower (c)) to compare the horizontal polysulfide distributions at different vertical locations, indicated in the filtered image of initial polysulfide distribution (d). The lithium foil surface is located at  $\sim$ 0.75 mm on the sample location axis.

**Sulfur quantification.**—The concentration of sulfur species was quantified using a  $CuS_x$  thin film standard that was mapped at the same energy, pixel size, and dwell time as the sulfur maps taken during cycling. All maps were normalized to the incoming X-ray beam hitting the sample to eliminate variations in pixel intensity due to incident beam intensity fluctuations. Because the  $CuS_x$  standard was measured in  $\mu g$  cm<sup>-2</sup>, the sulfur concentration is reported by area (i.e. mass/unit area). Area is used rather than volume because it cannot be assumed that the battery cell is homogeneous in depth, and the penetration depth is smaller than the depth of the battery cavity.

This limited penetration depth also accounts for some differences in concentration because sulfur species may be diffusing in and out of the penetration depth of the X-ray beam.

The maps were smoothed using SMAK's blur filtering algorithm with a filter size of three pixels and a blur standard deviation of one pixel. This method keeps the larger changes in concentration across the image while minimizing noise from individual high intensity pixels. After converting from intensity to concentration, three line cuts were taken in the polysulfide (2470.35 eV) maps, designated as upper, middle, and lower regions in Figures 7a, 7b, and 7c, respectively.

These graphs show the concentration of polysulfides across the separator and electrolyte region at Points (a), (f), (g), (i), and (r) in the cycling data. The line cuts plotted at the left are shown as a box in the image of initial polysulfide concentration from Point (a) in Figure 7d.

At Point (a), the concentration of polysulfides across the electrolyte is approximately constant in the upper, middle, and lower regions. At the end of the first discharge, Point (f), the concentration gradient slopes from a high value in the cathode to an elevated level closer to the lithium surface, located at  $\sim\!0.75$  mm on the sample location axis. In the upper region (Figure 7a), the concentration is approximately level in the middle of the separator. At Point (g), the beginning of the first charge, the concentration distribution is similar to that at Point (f) due to the electrochemical lag experienced by the cell when switching from discharge to charge that was also observed in the XANES fitting. However, there appears to be a slight decrease in the concentration at the edge of the electrode face in the middle region (Figure 7b). At the end of the first charge, Point (i), the relative concentrations at each interface again seem to level out across the electrolyte in the upper and middle regions (Figures 7a and 7b) but not in the lower region (Figure 7c); however, the absolute concentration has increased in all three areas. Again, this increase may be due to diffusion perpendicular to the plane of view. At the end of the third charge, Point (r), where the electrodes have lost most of their structure, the polysulfide concentration is once again minimized and approximately constant across the electrolyte. From these observations, we can conclude that while cycling, the polysulfide concentration remains higher in the sulfur cathode and decreases toward the lithium anode, even upon charging. The concentration returns to its initial state after the third cycle as the polysulfides begin to diffuse and equalize across the electrolyte.

### Conclusions

In this work, we demonstrated cross-sectional operando chemical mapping of lithium-sulfur batteries via a newly designed electrochemical cell. Using X-ray spectromicroscopy and a unique cell design, a spatially resolved picture of the changes in sulfur speciation was captured over three discharge/charge cycles. Observations included significant degradation of the electrode microstructure during cycling with substantial loss of active material at the end of three cycles. The area of polysulfide diffusion expands during the first discharge cycle and remains expanded throughout subsequent cycles, providing evidence that the sulfur species remain dissolved in the electrolyte and trapped in the separator, a potential cause of polysulfide shuttle. Additionally, XANES fitting showed that not all of the initial sulfur intensity was recovered upon charging and that polysulfides and lithium sulfide remain during additional cycles. At the end of the third charge, the primary species was Li<sub>2</sub>S<sub>8</sub> with some residual Li<sub>2</sub>S and minimal S<sub>8</sub>, suggesting that the reaction is only quasi-reversible and further proving the polysulfide shuttle effect.

Further work will include improvement of the cross-sectional cell electrochemistry to increase capacity as well as better time and spatial resolution for X-ray data collection to eliminate discontinuities in the maps. Because the area of interest for polysulfide diffusion in the cross-sectional design is between the sulfur electrode and the lithium metal, a more targeted mapping strategy with a finer step size in the glass fiber separator region will be used. The work presented here provides insight into the significant changes that can occur in a lithium-sulfur battery even during a few cycles. The chemistry of lithium-sulfur batteries is complex, and it is necessary to fully understand this chemistry to garner the true power of the lithium-sulfur system.

# Acknowledgments

Use of the Stanford Synchrotron Radiation Lightsource, SLAC National Accelerator Laboratory, is supported by the U.S. Department of Energy, Office of Science, Office of Basic Energy Sciences under Contract No. DE-AC02-76SF00515. This work was supported by the Joint Center for Energy Storage Research (JCESR), the Sony

Corporation, and the Battery500 Consortium. KNH was supported by the Science Undergraduate Laboratory Internship program. The authors thank Sam Webb and Courtney Roach for their assistance at BL 14-3.

#### ORCID

Elizabeth C. Miller https://orcid.org/0000-0002-8315-9361 Robert M. Kasse http://orcid.org/0000-0003-0738-744X Michael F. Toney http://orcid.org/0000-0002-7513-1166

#### References

- P. G. Bruce, S. A. Freunberger, L. J. Hardwick, and J.-M. Tarascon, *Nat. Mater.*, 11, 19 (2011).
- 2. L. F. Nazar, M. Cuisinier, and Q. Pang, MRS Bull., 39, 436 (2014).
- S. Zhang, K. Ueno, K. Dokko, and M. Watanabe, Adv. Energy Mater., 5, 1500117 (2015).
- R. D. Rauh, K. M. Abraham, G. F. Pearson, J. K. Surprenant, and S. B. Brummer, J. Electrochem. Soc., 126, 523 (1979).
- 5. H. Yamin, J. Electrochem. Soc., 135, 1045 (1988).
- A. Manthiram, Y. Fu, S. H. Chung, C. Zu, and Y. S. Su, Chem. Rev., 114, 11751 (2014).
- D. Bresser, S. Passerini, and B. Scrosati, Chem. Commun., 49, 10545 (2013).
- D. Lv, J. Zheng, Q. Li, X. Xie, S. Ferrara, Z. Nie, L. B. Mehdi, N. D. Browning, J. G. Zhang, G. L. Graff, J. Liu, and J. Xiao, Adv. Energy Mater., 5, 1 (2015).
- 9. H. Yao, G. Zheng, P.-C. Hsu, D. Kong, J. J. Cha, W. Li, Z. W. Seh, M. T. McDowell, K. Yan, Z. Liang, V. K. Narasimhan, and Y. Cui, Nat. Commun., 5, 4943 (2014).
- W. Li, Z. Liang, Z. Lu, H. Yao, Z. W. Seh, K. Yan, G. Zheng, and Y. Cui, Adv. Energy Mater., 5, 1500211 (2015).
- K. Dokko, N. Tachikawa, K. Yamauchi, M. Tsuchiya, A. Yamazaki, E. Takashima, J. Park, K. Ueno, S. Seki, N. Serizawa, and M. Watanabe, *J. Electrochem. Soc.*, 160, 32 (2013).
- 12. Z. Li, Y. Huang, L. Yuan, Z. Hao, and Y. Huang, Carbon N. Y., 92, 41 (2015)
- E. S. Shin, K. Kim, S. H. Oh, and W. Il Cho, *Chem. Commun. (Camb).*, 49, 2004 (2013).
- 14. N. Ding, X. Li, S. Chien, Z. Liu, and Y. Zong, Chem. Commun., 53, 10152 (2017).
- 15. Y. Diao, K. Xie, S. Xiong, and X. Hong, J. Power Sources, 235, 181 (2013).
- A. Rosenman, E. Markevich, G. Salitra, D. Aurbach, A. Garsuch, and F. F. Chesneau, Adv. Energy Mater., 5, 1 (2015).
- X. Tao, J. Wang, C. Liu, H. Wang, H. Yao, G. Zheng, Z. W. Seh, Q. Cai, W. Li, G. Zhou, C. Zu, and Y. Cui, *Nat. Commun.*, 7, 11203 (2016).
- M. J. Lacey, A. Yalamanchili, J. Maibach, C. Tengstedt, K. Edström, and D. Brandell, RSC Adv., 6, 3632 (2016).
- 19. X. Ji, S. Evers, R. Black, and L. F. Nazar, *Nat. Commun.*, **2**, 325 (2011).
- L. C. H. Gerber, P. D. Frischmann, F. Y. Fan, S. E. Doris, X. Qu, A. M. Scheuermann, K. Persson, Y. M. Chiang, and B. A. Helms, *Nano Lett.*, 16, 549 (2016).
- 21. S. Evers and L. F. Nazar, Acc. Chem. Res., 46, 1135 (2013).
- 22. J. Nelson Weker and M. F. Toney, Adv. Funct. Mater., 25, 1622 (2015).
- O. J. Borkiewicz, K. M. Wiaderek, P. J. Chupas, and K. W. Chapman, *J. Phys. Chem. Lett.*, 6, 2081 (2015).
- 24. S. S. Zhang, *Electrochim. Acta*, 97, 226 (2013).
- A. Kamyshny, A. Goifman, J. Gun, D. Rizkov, and O. Lev, *Environ. Sci. Technol.*, 38, 6633 (2004).
- L. A. Huff, J. L. Rapp, J. A. Baughman, P. L. Rinaldi, and A. A. Gewirth, Surf. Sci., 631, 295 (2015).
- K. A. See, M. Leskes, J. M. Griffin, S. Britto, P. D. Matthews, A. Emly, A. Van Der Ven, D. S. Wright, A. J. Morris, C. P. Grey, and R. Seshadri, *J. Am. Chem. Soc.*, 136, 16368 (2014).
- Y. Luo, W.-B. Cai, X. Xing, and D. A. Scherson, *Electrochem. Solid-State Lett.*, 7, E1 (2004).
- 29. H. L. Wu, L. A. Huff, and A. A. Gewirth, *ACS Appl. Mater. Interfaces*, 7, 1709 (2015).
- M. U. M. Patel, R. Demir-Cakan, M. Morcrette, J. M. Tarascon, M. Gaberscek, and R. Dominko, Chem.SusChem. 6, 1177 (2013).
- H. Marceau, C.-S. Kim, A. Paolella, S. Ladouceur, M. Lagacé, M. Chaker, A. Vijh, A. Guerfi, C. M. Julien, A. Mauger, M. Armand, P. Hovington, and K. Zaghib, J. Power Sources, 319, 247 (2016).
- S. Walué, C. Barchasz, J.-F. Colin, J.-F. Martin, E. Elkaim, J.-C. Leprêtre, and F. Alloin, Chem. Commun., 49, 7899 (2013).
- J. Nelson, S. Misra, Y. Yang, A. Jackson, Y. Liu, H. Wang, H. Dai, J. C. Andrews, Y. Cui, and M. F. Toney, *J. Am. Chem. Soc.*, 134, 6337 (2012).
- J. Conder, R. Bouchet, S. Trabesinger, C. Marino, L. Gubler, and C. Villevieille, Nat. Energy, 2, 17069 (2017).
- M. Cuisinier, P.-E. Cabelguen, S. Evers, G. He, M. Kolbeck, A. Garsuch, T. Bolin, M. Balasubramanian, and L. F. Nazar, "Sulfur Speciation in Li–S Batteries Determined by Operando X-ray Absorption Spectroscopy," *The Journal of Physical Chemistry Letters*, 4(19), 3227 (2013).
- Y. Gorlin, M. U. M. Patel, A. Freiberg, Q. He, M. Piana, M. Tromp, and H. a. Gasteiger, J. Electrochem. Soc., 163, A930 (2016).
- Y. Gorlin, A. Siebel, M. Piana, T. Huthwelker, H. Jha, G. Monsch, F. Kraus, H. A. Gasteiger, and M. Tromp, J. Electrochem. Soc., 162, A1146 (2015).
- R. Dominko, M. U. M. Patel, V. Lapornik, A. Vizintin, M. Kozelj, N. N. Tusar, I. Arcon, L. Stievano, and G. Aquilanti, J. Phys. Chem. C, 119, 19001 (2015).

- 39. Y. Ye, A. Kawase, M.-K. Song, B. Feng, Y.-S. Liu, M. Marcus, J. Feng, E. Cairns, J. Guo, and J. Zhu, *Nanomaterials*, **6**, 14 (2016).
- 40. A. Yermukhambetova, C. Tan, S. R. Daemi, Z. Bakenov, J. A. Darr, D. J. Brett, A. Tellindianickov, C. Tali, S. K. Dadini, Z. Datevi, S. L. Basil, E. Basil, S. Bas
- J. Cabana, J. Guo, M. Salmeron, and N. Balsara, J. Phys. Chem. Lett., 5, 1547 (2014).
- 42. K. H. Wujcik, T. A. Pascal, C. D. Pemmaraju, D. Devaux, W. C. Stolte, N. P. Balsara,
- and D. Prendergast, Adv. Energy Mater., 5 (2015).
  43. X. Feng, M.-K. Song, W. C. Stolte, D. Gardenghi, D. Zhang, X. Sun, J. Zhu, E. J. Cairns, and J. Guo, *Phys. Chem. Chem. Phys.*, 16, 16931 (2014).
- 44. W.-T. Xu, H.-J. Peng, J.-Q. Huang, C.-Z. Zhao, X.-B. Cheng, and Q. Zhang, "Towards Stable Lithium–Sulfur Batteries with a Low Self-Discharge Rate: Ion Diffusion Modulation and Anode Protection," ChemSusChem, 8, 2892 (2015).
- S. M. Webb, AIP Conf. Proc., 1365, 196 (2010).
   B. Ravel and M. Newville, J. Synchrotron Radiat., 12, 537 (2005).
- 47. Y. Orikasa, Y. Gogyo, H. Yamashige, M. Katayama, K. Chen, T. Mori, K. Yamamoto, T. Masese, Y. Inada, T. Ohta, Z. Siroma, S. Kato, H. Kinoshita, H. Arai, Z. Ogumi, and Y. Uchimoto, Sci. Rep., 6, 26382 (2016).
- W. Yang, Z. Wang, L. Chen, Y. Chen, L. Zhang, Y. Lin, J. Li, and Z. Huang, RSC Adv., 7, 33680 (2017).
- 49. Y. V. Mikhaylik and J. R. Akridge, J. Electrochem. Soc., 151, A1969 (2004).